Selected papers presented at the XIII All-Polish Seminar on Mössbauer Spectroscopy (OSSM 24)

Antiferromagnetic Ordering in VFeNbTiMo High-Entropy Alloy at Low Temperatures

P. Sobota[a,b,*], R. Idczak[a], R. Konieczny[a], W. Nowak[a,b] and V.H. Tran[b]

[a]*Institute of Experimental Physics, University of Wrocław, pl. M. Borna 9, 50-204 Wrocław, Poland*
[b]*Institute of Low Temperature and Structure Research, Polish Academy of Sciences, Okólna 2, 50-422 Wrocław, Poland*

Doi: 10.12693/APhysPolA.146.250 *e-mail: piotr.sobota2@uwr.edu.pl

Structural and physical properties of the VFeNbTiMo high-entropy alloy were studied by X-ray diffraction, scanning electron microscopy with energy dispersive X-ray spectroscopy, ^{57}Fe transmission Mössbauer spectroscopy, and magnetic measurements. It was found that the alloy forms two chemically distinct phases. The first, Mo-rich phase, crystallizes in a body-centered cubic structure (space group $Im\bar{3}m$) with $a = 3.1626(1)$ Å. The second, Fe-rich phase, crystallizes in a hexagonal structure (space group $P6_3/mmc$) with $a = 4.9245(2)$ Å, $c = 8.0419(5)$ Å. Magnetic measurements and ^{57}Fe transmission Mössbauer spectroscopy showed that the alloy is in a paramagnetic state at temperatures between 5 and 700 K. Below 5 K, the hexagonal Fe-rich phase undergoes an antiferromagnetic transition.

topics: high-entropy alloys, Mössbauer spectroscopy, magnetism

1. Introduction

The high-entropy alloys (HEAs) can be defined as solid solutions of five or more metals mixed in non-negligible proportions [1, 2]. One of the defining factors of HEA is that its value of configurational entropy (ΔS_{config}) should generally be close to, or larger than, $1.5R$ (where R is a universal gas constant). High-entropy alloys have attracted much attention in recent years due to their excellent mechanical properties [3] (also at cryogenic temperatures [4]) and chemical resistance [5]. According to the work by Yeh et al. [2], these properties are a result of several key effects associated with HEA: thermodynamic stabilization of the single phase by high-entropy effect, slow diffusion resulting in retardation of second phase growth, strong lattice distortions causing extensive strength and slow kinetics, and the so-called cocktail effect. Despite that, multiple works report the presence of the multi-phase HEAs. In the case of these materials, it is often hard to properly describe the separate properties of each phase [6, 7], especially in the case of magnetic properties [8].

However, for Fe-rich materials, ^{57} Fe Mössbauer spectroscopy offers many advantages as a valuable method for the characterization of samples containing iron atoms. In particular, Mössbauer spectroscopy is very sensitive to the local electronic and chemical environment around the ^{57}Fe Mössbauer probes [9, 10]. As was shown in several reports concerning the study of high-entropy alloys using Mössbauer spectroscopy [11–13], this technique is very helpful in the identification and characterization of multi-phase HEAs containing iron.

In this paper, we present the results of the synthesis of the new high-entropy alloy VFeNbTiMo, along with analysis by X-ray diffraction (XRD), scanning electron microscopy with energy dispersive X-ray spectroscopy (SEM-EDXS), bulk magnetic measurement at low temperatures, and transmission Mössbauer spectroscopy (TMS) in a temperature range of 1.7–700 K.

2. Experimental details

A polycrystalline sample of VFeNbTiMo high-entropy alloy was obtained by conventional arc melting of elemental metals (of purity minimum of 99.9%) under Ti gettered Ar atmosphere. During the synthesis, to increase homogeneity, the sample was repeatedly flipped and remelted four times. The mass loss (defined by the mass difference between raw materials and the final alloy) was below 0.2%, which is a negligible amount in the case of HEAs.

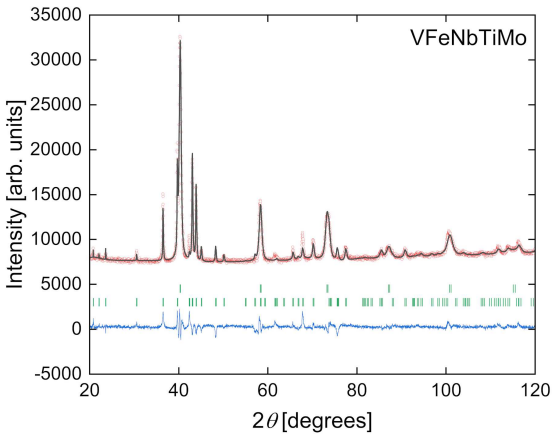

Fig. 1. X-ray diffraction pattern and results of Rietveld refinement of VFeNbTiMo alloy. Red dots and black lines represent the experimental data and the theoretical curves, respectively. The blue line shows the difference between the two, and green dashes indicate the positions of the Bragg reflections. The top line of dashes represents the Bragg reflections of the cubic phase, while the hexagonal phase's Bragg reflections are in the bottom line.

To facilitate the measurements, the sample was cut using a circular saw. Then, some parts of it were grounded in agate mortar into fine powder for the XRD and TMS measurements.

The crystal structure of the as-obtained product was examined by powder XRD using a PANalytical X'pert PRO diffractometer with Cu K_α radiation. The experimental XRD pattern was analyzed by the Rietveld method using the FullProf software [14]. All the referential crystallographic data were taken from the Materials Project database [15].

The chemical composition and homogeneity of the sample were verified by SEM-EDXS using a field emission scanning electron microscope (FE-SEM) FEI Nova NanoSEM 230 equipped with an EDAX Genesis XM4 spectrometer on the surface of the cut specimen.

Magnetic properties of the alloy were studied in temperatures from 1.72 to 300 K and in nominal magnetic field $\mu_0 H = 5$ mT using a commercial Quantum Design MPMS-XL magnetometer.

The ^{57}Fe TMS spectra were recorded by a conventional constant-acceleration spectrometer, using a standard ^{57}Co-in-Rh source with a full width at half maximum (FWHM) of 0.22 mm/s. Spectra measured at temperatures 1.7–300 K were collected using a variable-temperature insert in an Oxford Instruments Spectromag cryostat. In the temperature range of 300–700 K, the measurements were performed using a standard Mössbauer furnace. The obtained spectra were analyzed using a least-squares fitting procedure, which provides the values of hyperfine interaction parameters such as isomer shift (IS), quadrupole splitting/shift (QS), hyperfine field B, as well as the relative intensities (C) and FWHM (Γ) of spectral lines. All IS values presented in this work are related to the IS value of α-Fe measured at room temperature.

3. Results and discussion

Figure 1 shows the XRD pattern obtained for the VFeNbTiMo alloy along with the results of Rietveld refinement. The analysis of the XRD pattern indicates the presence of two major phases. One crystallizes in body-centered cubic (bcc) structure with the lattice parameter $a = 3.1626(1)$ Å (space group $Im\bar{3}m$, W-type structure). The second one crystallizes in a hexagonal structure (space group $P6_3/mmc$) with lattice parameters $a = b = 4.9245(2)$ Å, $c = 8.0419(5)$ Å.

For the phase crystallizing in bcc structure in the $Im\bar{3}m$ space group, the a parameter seems to be close to the average a value of constituent metals of the alloy crystallizing in the same space group: Fe (2.86 Å), V (2.98 Å), Mo (3.17 Å), Ti (3.25 Å), Nb (3.32 Å). This can indicate that, in fact, it is a HEA phase.

To perform the correct analysis of the collected XRD pattern, it is necessary to take into account the results of EDXS and TMS measurements, which are presented later in the article. Using the results of EDXS measurements, we were able to determine the chemical composition of both phases, which were labeled as Mo-rich phase and Fe-rich phase. By applying Vengard's law of mixing and using at.% contents as the weights, we estimated that the Mo-rich phase would have lattice parameter a very close (3.1534 Å) to the a parameter of the bcc phase (3.1626(1) Å) detected from the XRD measurement. This result allows us to ascribe the bcc phase to the Mo-rich phase and, by elimination, the hexagonal phase to the Fe-rich phase.

At the same time, the structural information derived from the TMS measurements indicates that the iron atoms in each phase occupy only a single site. While this is unsurprising for the bcc phase, it shows that the hexagonal phase is partially ordered (as it has three Wyckoff positions — $2a$, $4f$, $6h$ — that Fe atoms can potentially occupy). Similar partial segregation can be observed in the isostructural $Re_{0.56}Nb_{0.11}Ti_{0.11}Zr_{0.11}Hf_{0.11}$ high-entropy alloy [16] and was then taken into account when solving the presented structure. In the case of the hexagonal phase in VFeNbTiMo alloy, the Rietveld analysis indicates that Fe atoms occupy a $6h$ position along with other elements, mostly Nb and V. Position $4f$ is occupied by Ti and Mo, and position $2a$ by Nb and V. The resulting fit is of good quality, which is indicated by the reliability factors (not corrected for the background): $R_{\mathrm{exp}} = 1.08$ and $R_{\mathrm{wp}} = 2.52$.

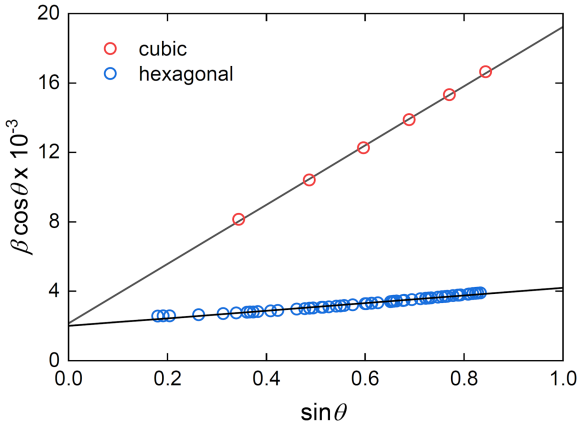

Fig. 2. The Williamson–Hall plots, where solid black lines are linear fits, according to (1), to experimental points marked as red (cubic phase) and blue (hexagonal phase) circles.

TABLE I

Compositions of phases measured by EDXS.

	Element [at.%]				
	Ti	V	Fe	Nb	Mo
Nominal	20	20	20	20	20
All surface	18.7(7)	19.2(8)	19.3(8)	21.5(4)	21.3(4)
Fe-rich phase	21.8(6)	19(1)	29(2)	17.8(2)	12.4(7)
Mo-rich phase	15.4(1)	18.9(8)	10.1(7)	23.1(2)	32.6(2)

The Rietveld refinement and EDXS data also allowed us to determine the weight fractions of the phases: 61 wt% (bcc) and 39 wt% (hexagonal). From that, the molar fractions (bcc: 57 at.%, hexagonal: 43 at.%) and the relative concentration of Fe in the alloy phases were calculated. The bcc phase contains 31% and the hexagonal phase 69% of Fe atoms in the sample.

The Williamson–Hall method was applied to determine the average crystalline size L along with the average lattice strain ϵ of the phases in the studied sample. Using the data obtained from Rietveld refinement of the obtained XRD pattern, a linear fit was applied according to the following formula [17]

$$\beta\cos(\theta) = \epsilon\sin(\theta) + \frac{K\lambda}{L}, \qquad (1)$$

where β is the full width at half maximum (FWHM) intensity in 2θ units, θ is the Bragg angle, λ is the X-ray wavelength, and $K = 0.9$ is the shape factor. The results are presented in Fig. 2. The average crystalline size $L = 64(4)$ nm and average lattice strain $C\epsilon = 1.71(2)\%$ were determined for the cubic phase, while for the hexagonal phase, they are $L = 69(1)$ nm and $C\epsilon = 0.22(1)\%$.

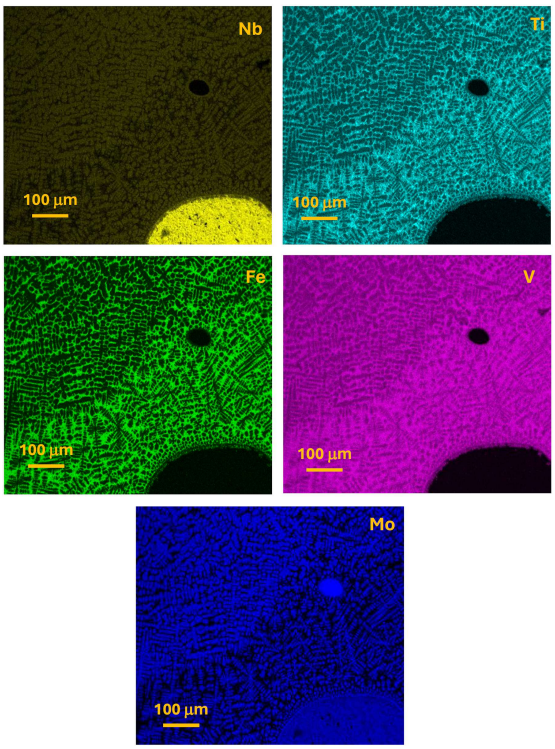

Fig. 3. The SEM micrographs of the surface of the sample VFeNbTiMo with EDXS maps superimposed on them.

To further analyze the structure, homogeneity, and morphology of the phases in the prepared sample, the SEM-EDXS mapping was conducted for the surface of the cut specimen.

The micrographs with superimposed EDXS maps are presented in Fig. 3. The analysis of the pictures reveals the presence of two chemically distinct phases. Additionally, some precipitates or unmelted fragments of Nb and Mo are visible, but their abundance in the volume of the sample must be low, since they were not detected by the XRD method.

The results of the EDXS analysis are presented in Table I. The data collected from the whole surface show that the average element content is close to nominal values. The point EDXS analysis of two distinct phases revealed a large disproportion of elements between those phases, especially in regard to Mo and Fe. The two major phases are corresponding to the structures detected by the XRD. However, the distribution of the two phases throughout the sample's volume appears to be uneven.

The temperature dependence of the mass susceptibility χ_{mass} measured in a field of $\mu_0 H = 5$ mT for the VFeNbTiMo sample is presented in Fig. 4. The behavior of $\chi_{\mathrm{mass}}(T)$ between 5 and 300 K indicates a local-moment paramagnetism contributed from the iron atoms. No anomaly around 9 K (the superconducting critical temperature of Nb) is visible, which further proves that the amount of niobium precipitates in the sample is minuscule.

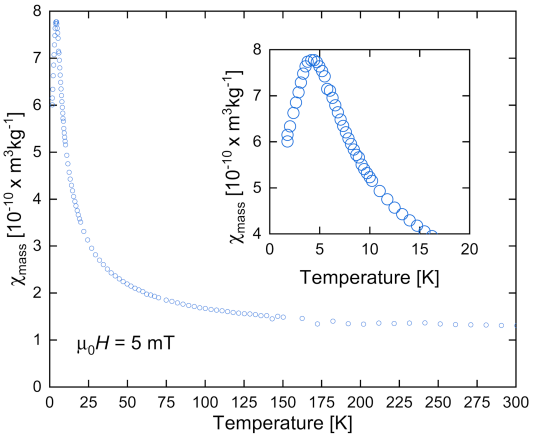

Fig. 4. The temperature dependence of mass susceptibility measured for the VFeNbTiMo sample. Insert shows low-temperature range.

Below $T = 5$ K, the χ_{mass} values start to decrease with lowering temperatures, revealing that the sample undergoes the antiferromagnetic transition at Néel temperature $T_{\text{N}} = 4.7(2)$ K. As it is unlikely that both phases have similar transition temperature, the TMS measurements of the studied system were performed down to 1.7 K. The Mössbauer data should give an answer as to which phase undergoes the magnetic transition below 5 K.

The selected TMS spectra collected for the VFeNbTiMo sample at temperatures between 1.7 and 700 K are presented in Figs. 5 and 6. As one can notice, all spectra were described by two components. The first, single line component (singlet), can be ascribed to the Fe atoms located in the bcc Mo-rich phase, since it is accepted that the QS parameter in the cubic lattice should be equal to zero [9, 10]. However, it should be noted that the magnetic interaction can lead to a weak electric field gradient (magnetostriction) even in a cubic structure, e.g., in bcc α-Fe [18]. The second component, the quadrupole splitting doublet with QS close to $-0.26(1)$ mm/s at room temperature, can be connected to the presence of iron atoms in the hexagonal Fe-rich phase. The sign of QS was determined after the appearance of hyperfine magnetic interaction in spectra measured at the lowest temperatures (described later). The relative intensities of both components are $C_{\text{bcc}} = 25(1)\%$ and $C_{\text{hex}} = 75(1)\%$, which is a result comparable with our previous finding that the bcc phase contains 31% and the hexagonal phase 69% of Fe atoms in the sample. At the same time, only one component assigned to the hexagonal phase indicates that iron atoms occupy only one crystallographic site in this structure. As was mentioned, this result was taken into account in XRD data analysis. The FWHM of spectral lines of both components do not vary with temperature, and they were close to $\Gamma_{\text{bcc}} = 0.32(2)$ mm/s and $\Gamma_{\text{hex}} = 0.29(2)$ mm/s.

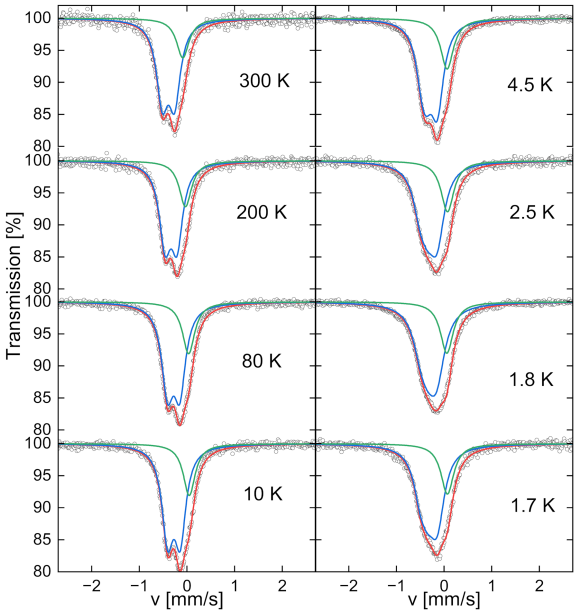

Fig. 5. The selected TMS spectra collected for the VFeNbTiMo sample at temperatures between 1.7 and 300 K. Solid lines are fits, as described in the text.

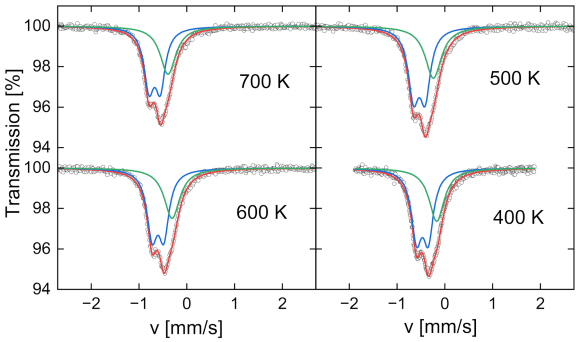

Fig. 6. The selected TMS spectra collected for the VFeNbTiMo sample at temperatures between 300 and 700 K. Solid lines are fits, as described in the text.

As one can notice in Fig. 5, the shapes of TMS spectra measured below 5 K are different from those collected in the temperature range of 10–700 K. In particular, the component assigned to the hexagonal phase becomes broad and can be described by an unresolved (collapsed) Zeeman six-line pattern (sextet). The determined QS parameter does not vary with temperature and is close to $-0.26(1)$ mm/s. At the same time, the estimated hyperfine field B increases with decreasing temperature. At 4.5 K, $B = 0.31(1)$ T while at 1.7 K, $B = 0.46(2)$ T. Despite the fact that the determined B values are relatively small, similar findings were presented in the case of Mössbauer studies of antiferromagnetism of an iron-rich hexagonal close-packed (hcp) alloys such as Fe–Mn [19, 20], Fe–Ru and Fe–Os [21]. According

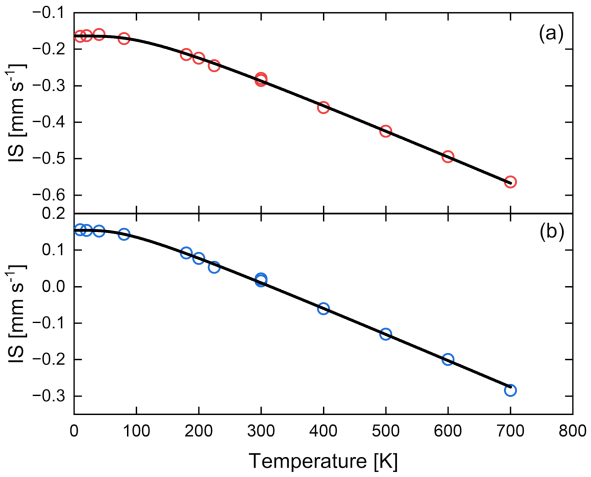

Fig. 7. The temperature dependence of IS_{hex} (red points) and IS_{bcc} (blue points) parameters derived from TMS spectra measured for the VFeNbTiMo sample. The solid lines represent the fit of experimental values to (2). The standard uncertainties for the presented quantities do not exceed 1%.

to these works, the antiferromagnetism founded in iron-rich hcp alloys is probably due to itinerant electron polarization. Consequently, hcp alloys have much weaker internal magnetic fields than observed for bcc Fe, and the small magnetic moment of iron atoms may be attributed to a weaker exchange interaction in the hcp lattice than in the bcc lattice.

The variation of IS_{bcc} and IS_{hex} parameters with temperature is presented in Fig. 7. Above 5 K, the determined experimental values decrease concavely with temperature due to the second-order Doppler (SOD) effect [9, 10]. Since then, the temperature dependencies of IS_{bcc} and IS_{hex} can be expressed in terms of the Debye approximation of the lattice vibrations as [10]

$$IS(T) = IS(0) - \frac{9}{2}\frac{k_{\mathrm{B}}T}{cM}\left(\frac{T}{\Theta_{\mathrm{D}}}\right)^3 \int_0^{\Theta_{\mathrm{D}}/T} \frac{\mathrm{d}x\, x^3}{\mathrm{e}^x - 1}, \tag{2}$$

where $IS(0)$ denotes the temperature-independent isomer shift, k_{B} is the Boltzmann constant, M is the mass of ^{57}Fe, c is the speed of light in vacuum, and Θ_{D} stands for the Debye temperature. Fitting experimental data to (2) yields $IS_{\mathrm{bcc}}(0) = 0.154(3)$ mm/s and $\Theta_{\mathrm{D}}^{\mathrm{bcc}} = 319(19)$ K for bcc phase and $IS_{\mathrm{hex}}(0) = -0.164(2)$ mm/s and $\Theta_{\mathrm{D}}^{\mathrm{hex}} = 429(12)$ K for hexagonal phase. It is worth noting that the estimated $\Theta_{\mathrm{D}}^{\mathrm{hex}}$ is very close to Θ_{D} determined for hcp Ti (420 K) [22] and hcp Fe (422 K) [23], which are the main elements of the hexagonal phase. In the case of $\Theta_{\mathrm{D}}^{\mathrm{bcc}} = 319(19)$ K, this value is comparable to $\Theta_{\mathrm{D}} = 367$ K calculated using the mixing rule and Debye temperatures of pure bcc Fe (477 K), V (399 K), Mo (423 K), Nb (276 K), and Ti (269 K) [22, 24].

Below 5 K, the values of IS_{bcc} increase and the values of IS_{hex} decrease with lowering temperature. This finding indicates that the electronic structure of both phases observed in the VFeNbTiMo sample changes due to the magnetic transition.

4. Conclusions

A new multi-phase HEA VFeNbTiMo was synthesized using the arc melting method. The analysis of XRD data, SEM micrographs, and EDXS maps indicates that the alloy forms two chemically distinct phases that crystallize in body-centered cubic and hexagonal structures. Magnetic measurements showed that the studied system undergoes the antiferromagnetic transition at Néel temperature $T_{\mathrm{N}} = 4.7(2)$ K. ^{57}Fe transmission Mössbauer spectroscopy confirms this finding and additionally reveals that below 5 K, only the hexagonal Fe-rich phase undergoes a magnetic transition.

Acknowledgments

This work was co-financed by the National Science Center (Poland) under the OPUS 20 project number 2020/39/B/ST5/01782.

References

[1] B. Cantor, *Prog. Mater. Sci.* **120**, 100754 (2021).

[2] J.-W. Yeh, S.-K. Chen, S.-J. Lin, J.-Y. Gan, T.-S. Chin, T.-T. Shun, C.-H. Tsau, S.-Y. Chang, *Adv. Eng. Mater.* **6**, 299 (2004).

[3] K.M. Youssef, A.J. Zaddach, C. Niu, D.L. Irving, C.C. Koch, *Mater. Res. Lett.* **3**, 95 (2015).

[4] B. Gludovatz, A. Hohenwarter, D. Catoor, E.H. Chang, E.P. George, R.O. Ritchie, *Science* **345**, 1153 (2014).

[5] Y. Chen, U. Hong, J. Yeh, H. Shih, *Scr. Mater.* **54**, 1997 (2006).

[6] Y. Yu, J. Wang, J. Li, H. Kou, W. Liu, *Mater. Lett.* **138**, 78 (2015).

[7] P. Sobota, R. Topolnicki, T. Ossowski, T. Pikula, D. Gnida, R. Idczak, A. Pikul, *Sci. Rep.* **13**, 16317 (2023).

[8] Q. Lan, A. Kovács, J. Caron et al., *iScience* **25**, 104047 (2022).

[9] N. Greenwood, T. Gibb, *Mössbauer Spectroscopy*, John Wiley & Sons, 1971.

[10] P. Gütlich, E. Bill, A. Trautwein, *Mössbauer Spectroscopy and Transition Metal Chemistry: Fundamentals and Applications*, Springer, Berlin 2010.

[11] A. Perrin, M. Sorescu, V. Ravi, D.E. Laughlin, M.E. McHenry, *AIP Adv.* **9**, 035329 (2019).

[12] P. Sliwa, K. Berent, J. Przewoznik, J. Cieslak, *J. Alloys Compd.* **814**, 151757 (2020).

[13] J. Cieslak, M. Calvo-Dahlborg, K. Berent, U. Dahlborg, *J. Magn. Magn. Mater.* **518**, 167371 (2021).

[14] J. Rodríguez-Carvajal, *Physica B* **192**, 55 (1993).

[15] A. Jain, S.P. Ong, G. Hautier, W. Chen, W.D. Richards, S. Dacek, S. Cholia, D. Gunter, D. Skinner, G. Ceder, K.A. Persson, *APL Mater.* **1**, 011002 (2013).

[16] S. Marik, K. Motla, M. Varghese, K.P. Sajilesh, D. Singh, Y. Breard, P. Boullay, R.P. Singh, *Phys. Rev. Mater.* **3**, 060602 (2019).

[17] G. Williamson, W. Hall, *Acta Metall.* **1**, 22 (1953).

[18] A. Błachowski, K. Komędera, K. Ruebenbauer, G. Cios, J. Zukrowski, R. Górnicki, *J. Alloys Compd.* **673**, 420 (2016).

[19] C. Kimball, W.D. Gerber, A. Arrott, *J. Appl. Phys.* **34**, 1046 (1963).

[20] H. Ohno, M. Mekata, *J. Phys. Soc. Jpn.* **31**, 102 (1971).

[21] H. Ohno, *J. Phys. Soc. Jpn.* **31**, 92 (1971).

[22] A. Tari, *The Specific Heat of Matter at Low Temperatures*, Imperial College Press, London 2003.

[23] S. Sharma, *Solid State Commun.* **149**, 2207 (2009).

[24] Q. Chen, B. Sundman, *Acta Mater.* **49**, 947 (2001).